

# Linear stability analysis of rapid granular flow on a slope and density wave formation

By **NAMIKO MITARAI AND HIZU NAKANISHI**

Department of Physics, Kyushu University 33, Fukuoka 812-8581, Japan

(Received 22 May 2019)

The linear stability of rapid granular flow on a slope under gravity is analyzed using hydrodynamic equations. It is demonstrated that the steady uniform flow becomes unstable against the long-wavelength perturbations longitudinal to the flow direction for a certain parameter range to form the density wave. The results are compared with our previous molecular dynamics simulations (Mitarai & Nakanishi 2001), where the spontaneous density wave formation has been found.

---

## 1. Introduction

Granular flow exhibits a variety of dynamical phenomena, which have been attracting research interests for years (Jaeger, Nagel & Behringer 1996). Its complex behaviors can be seen even in a simple situation like the gravitational flow on a slope. When the inclination angle is large and the slope is rough, a rapid and relatively low-density flow is realized, and the interaction between grains is dominated by inelastic collisions. On the other hand, when the inclination angle is small, the flow becomes dense and slow, and the frictional interaction plays an important role (Mitarai & Nakanishi 2003). The comprehensive rheology of the granular flow has not been established yet, except for the rapid collisional flow regime, where the hydrodynamic models have been developed with the constitutive relations based on the kinetic theory of inelastic hard spheres (Jenkins & Savage 1983; Campbell 1990; Lun *et al.* 1984); it has been demonstrated that a certain quantitative agreement can be achieved for the uniform flow by introducing the spinning motion of each grains (Mitarai, Hayakawa & Nakanishi 2002). The uniform granular flow, however, turns out to be unstable in various ways, and shows rich phenomena.

In the experiment on a shallow granular flow on a wide slope, Forterre & Pouliquen (2001) have observed that there appears a regular pattern of longitudinal streaks along the flowing direction. This phenomenon has been analyzed by means of the hydrodynamic equations for rapid granular flow (Forterre & Pouliquen 2002). They have calculated the steady uniform solutions and examined its linear stability numerically. They have found that, at a certain parameter region, the steady flow shows the “inverted density profiles”, in which the maximum density appears not at the bottom but at a finite distance from the bottom because of the agitation by the collisions with the rough solid bottom. It has been shown that the solutions with the “inverted density profiles” are unstable against the perturbations transverse to the flowing direction, and the instability results in the vortex patterns analogous to the rolls in the Rayleigh-Bernard convection; the streaks found in the experiment were interpreted as the result of the rolls of vortices.

Another instability that has been observed is the density wave formation along the flowing direction; experimentally, Louge & Keast (2001) have observed the jamming patterns traveling upstream in the dense chute flow, and Prasad, Pal & Römkens (2000) have

found the waves develops in the shallow flow as they travel downstream. The present authors have performed the molecular dynamics simulations of two-dimensional granular flow on a slope and found that the uniform flows are unstable against the density wave formation when the length of the slope is long enough and/or the particle density is low enough (Mitarai & Nakanishi 2001).

The purpose of this paper is to perform the linear stability analysis on the hydrodynamic equations to investigate the nature of the density wave formation instability found in the experiments and the numerical simulations. The basic method is the same with that used in Forterre & Pouliquen(2002), but we examine the stability against the perturbations longitudinal to the flowing direction in contrast with the case of Forterre & Pouliquen(2002), where the transverse stability has been studied.

This paper is organized as follows. In §2, the hydrodynamic model for rapid granular flow is introduced. The steady uniform solutions are numerically obtained in §3, and the results of the linear stability analysis is presented in §4. In §5, discussions and the comparison with the molecular dynamics simulations are given. The results are summarized in §6.

## 2. Hydrodynamic Equations for Granular Flows

### 2.1. Hydrodynamic equations and constitutive relations

The hydrodynamic fields for granular flows in three dimension are the mass density  $\rho$ , the mean velocity  $\mathbf{u}$ , and the granular temperature  $T$ , where  $T = \langle \delta \mathbf{u}^2 \rangle / 3$ . Here,  $\delta \mathbf{u} = \mathbf{u} - \langle \mathbf{u} \rangle$  and  $\langle \dots \rangle$  represents the average over the microscopic scale. Under gravity, they follow

$$\left( \frac{\partial}{\partial t} + \mathbf{u} \cdot \nabla \right) \rho = -\rho \nabla \cdot \mathbf{u}, \quad (2.1)$$

$$\rho \left( \frac{\partial}{\partial t} + \mathbf{u} \cdot \nabla \right) \mathbf{u} = \rho \mathbf{g} - \nabla \cdot \Sigma, \quad (2.2)$$

$$\frac{3}{2} \rho \left( \frac{\partial}{\partial t} + \mathbf{u} \cdot \nabla \right) T = -\nabla \cdot \mathbf{q} - \Sigma \cdot \nabla \mathbf{u} - \Gamma, \quad (2.3)$$

with the acceleration of gravity  $\mathbf{g}$ , the stress tensor  $\Sigma$ , the heat flux  $\mathbf{q}$ , and the energy loss  $\Gamma$  due to the inelastic nature of interactions between grains.

We employ the constitutive relations derived by Lun *et al.*(1984) for three dimensional system based on the kinetic theory of the inelastic particles: †

$$\Sigma = (p - \zeta \nabla \cdot \mathbf{u}) I - 2\mu S, \quad (2.4)$$

$$\mathbf{q} = -\kappa \nabla T, \quad (2.5)$$

where

$$S = \frac{1}{2} [\nabla \mathbf{u} + {}^t (\nabla \mathbf{u})] - \frac{1}{3} (\nabla \cdot \mathbf{u}) I, \quad (2.6)$$

and

$$\begin{aligned} p(\nu, T) &= \rho_p f_1(\nu) T, & \mu(\nu, T) &= \rho_p \sigma f_2(\nu) T^{1/2}, & \zeta(\nu, T) &= \rho_p \sigma f_3(\nu) T^{1/2}, \\ \kappa(\nu, T) &= \rho_p \sigma f_4(\nu) T^{1/2}, & \Gamma(\nu, T) &= \frac{\rho_p}{\sigma} (1 - e_p^2) f_5(\nu) T^{3/2}, \end{aligned} \quad (2.7)$$

† The original form of  $\mathbf{q}$  derived by Lun *et al.*(1984) is  $\mathbf{q} = -\kappa \nabla T - \kappa_h \nabla \nu$ . The coefficient  $\kappa_h$  is proportional to  $(1 - e_p)$ , thus disappears in the elastic limit. We checked that the influence of the term  $\kappa_h \nabla \nu$  on the steady solutions are small in the considered parameter region, and neglect this term as Forterre & Pouliquen(2002).

---


$$\begin{aligned}
f_1(\nu) &= \nu(1 + 4\eta\nu g_0(\nu)) \\
f_2(\nu) &= \frac{5\pi^{1/2}}{96\eta(2-\eta)} \left(1 + \frac{8}{5}\eta\nu g_0(\nu)\right) \left(\frac{1}{g_0(\nu)} + \frac{8}{5}\eta(3\eta-2)\nu\right) + \frac{8}{5\pi^{1/2}}\eta\nu^2 g_0(\nu) \\
f_3(\nu) &= \frac{8}{3\pi^{1/2}}\eta\nu^2 g_0(\nu) \\
f_4(\nu) &= \frac{25\pi^{1/2}}{16\eta(41-33\eta)} \left(1 + \frac{12}{5}\eta\nu g_0(\nu)\right) \left(\frac{1}{g_0(\nu)} + \frac{12}{5}\eta^2(4\eta-3)\nu\right) + \frac{4}{\pi^{1/2}}\eta\nu^2 g_0(\nu) \\
f_5(\nu) &= \frac{12}{\pi^{1/2}}\nu^2 g_0(\nu) \\
f_6(\nu) &= \frac{\sqrt{3}\pi\nu g_0(\nu)}{2\nu_m f_4(\nu)} \\
f_7(\nu) &= \frac{\pi\nu g_0(\nu)}{2\sqrt{3}\nu_m f_2(\nu)}
\end{aligned}$$

TABLE 1. Dimensionless functions used in the constitutive relations and the boundary conditions with  $\eta \equiv (1 + e_p)/2$ .

---

with the material density of particle  $\rho_p$ , the packing fraction  $\nu = \rho/\rho_p$ , the particle diameter  $\sigma$ , and the restitution coefficient between particles  $e_p$ . Here,  $I$  represents the unit matrix. The dimensionless functions  $f_i(\nu)$  ( $i = 1, \dots, 5$ ) are given in Table 1. For the radial distribution function  $g_0(\nu)$  in these functions, we adopted the form suggested by Lun & Savage(1986):

$$g_0(\nu) = \frac{1}{(1 - \nu/\nu_m)^{2.5\nu_m}}, \quad (2.8)$$

with the maximum solid fraction  $\nu_m$ , for which we use 0.60 as Forterre & Pouliquen(2002).

In the following, all the variables are non-dimensionalized by the length unit  $\sigma$ , the mass unit  $\rho_p\sigma^3$ , and the time unit  $\sqrt{\sigma/g}$ . The density field is expressed by the packing fraction  $\nu$  instead of the mass density  $\rho$ . The restitution coefficient between particles is set to be  $e_p = 0.7$ , that is the value used in our previous simulations (Mitarai & Nakanishi 2001).

## 2.2. Boundary conditions

The granular flow has a non-zero slip velocity at the solid boundary, where we should impose the momentum and the kinetic energy balances. Sophisticated boundary conditions have been proposed based on microscopic calculations of the kinetic theory for specific geometries (Jenkins & Richman 1986; Richman 1988; Jenkins 1992). We employ, however, a simpler form of the boundary condition obtained from a heuristic approach (Johnson & Jackson 1987; Johnson, Nott & Jackson 1987);

$$-\mathbf{n} \cdot \Sigma \cdot \mathbf{t} = \eta^*(\nu, T) |\mathbf{u}_s|, \quad (2.9)$$

$$\mathbf{n} \cdot \mathbf{q} = -\mathbf{u}_s \cdot \Sigma \cdot \mathbf{n} - \Gamma^*(\nu, T), \quad (2.10)$$

where the unit vector  $\mathbf{n}$  is normal to the floor,  $\mathbf{u}_s$  is the slip velocity at the floor, and  $\mathbf{t} = \mathbf{u}_s/|\mathbf{u}_s|$  is the unit vector along the slip velocity.

The first equation (2.9) expresses that the stress at the boundary balances with the

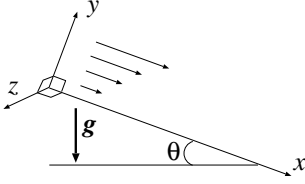


FIGURE 1. The coordinate system.

momentum transfer due to the collisions between the slope and the flowing grains. The momentum transfer, or RHS of (2.9), is assumed to be given by

$$\eta^*(\nu, T)|\mathbf{u}_s| = \phi m |\mathbf{u}_s| \Omega(\nu, T), \quad (2.11)$$

with the particle mass  $m$  and the collision rate  $\Omega(\nu, T)$  per unit time per unit area. The parameter  $\phi$  characterizes the roughness of the boundary, and the expression means that the fraction  $\phi$  of the particle momentum is transferred to the boundary in each collision, therefore, the larger value of  $\phi$  represents the rougher boundary. For the rough boundary in the two-dimensional system with closed packed disks, Jenkins & Richman(1986) estimated as  $\phi \sim 0.1$ , but Forterre & Pouliquen(2002) adopted the smaller value  $\phi = 0.05$  for most of the cases because they expected that a boundary with closed packed spheres in three-dimensional system is smoother on average. In this paper, we mainly use  $\phi = 0.05$ , but the case of  $\phi = 0.10$  is also examined in order to see general tendency.

The second equation (2.10) represents the energy balance, and means that the heat flux at the boundary comes from two effects, namely, the frictional heating due to the non-zero slip velocity and the energy loss due to the inelastic collision with the floor. The energy loss term  $\Gamma^*$  in (2.10) is given by

$$\Gamma^* = \Phi \frac{m}{2} < \delta \mathbf{u}^2 > \Omega(\nu, T) \quad (2.12)$$

with the collision rate  $\Omega(\nu, T)$ . The parameter  $\Phi$  represents the rate of energy loss per collision<sup>†</sup>, and we use  $\Phi = 0.39$  in this paper.

For the collision rate  $\Omega(\nu, T)$ , we use the form adopted by Forterre & Pouliquen(2002), then the expression of  $\eta^*(\nu, T)$  and  $\Gamma^*(\nu, T)$  in non-dimensionalized form are

$$\eta^*(\nu, T) = \phi f_7(\nu) f_2(\nu) T^{1/2}, \quad (2.13)$$

$$\Gamma^*(\nu, T) = \frac{1}{2} \Phi f_6(\nu) f_4(\nu) T^{3/2}, \quad (2.14)$$

where the dimensionless functions  $f_6(\nu)$  and  $f_7(\nu)$  are given in Table 1.

At infinity, we impose the condition that the stress and the heat flux vanish, namely,

$$\Sigma \rightarrow 0 \quad \text{and} \quad \mathbf{q} \rightarrow 0 \quad \text{as} \quad y \rightarrow \infty, \quad (2.15)$$

where the  $y$  axis is taken perpendicular to the floor (figure 1).

<sup>†</sup> Johnson & Jackson(1987) explicitly relate  $\Phi$  to the restitution coefficient between the floor and the particles  $e_w$  in the form  $\Phi = (1 - e_w^2)$ , but we adopt (2.12) as a more general expression.

### 3. Steady Uniform Flows

#### 3.1. Equations and Numerical method

First, we consider the steady solution which is uniform along the slope for (2.1) - (2.3) with the boundary conditions (2.9), (2.10), and (2.15) in the form

$$\nu(x, y, z, t) = \nu_0(y), \quad (3.1)$$

$$\mathbf{u}(x, y, z, t) = (u_0(y), 0, 0), \quad (3.2)$$

$$T(x, y, z, t) = T_0(y), \quad (3.3)$$

where we take the  $x$  axis along the slope, the  $y$  axis perpendicular to the floor, and the  $z$  axis perpendicular to the  $x - y$  plane (figure 1).

Then, the equations (2.1) - (2.3) are written as

$$0 = \nu_0 g \sin \theta - \frac{d\Sigma_{xy}^0}{dy}, \quad (3.4)$$

$$0 = -\nu_0 g \cos \theta - \frac{d\Sigma_{yy}^0}{dy}, \quad (3.5)$$

$$0 = -\Sigma_{xy}^0 \frac{du_0}{dy} - \frac{dq_y^0}{dy} - \Gamma^0, \quad (3.6)$$

where the superscript 0 denotes that the functions are for the steady solution, namely,  $\mathbf{q}^0 = -\kappa(\nu_0, T_0) \nabla T_0 = (0, q_y^0, 0)$ , etc. By integrating (3.4) and (3.5) over  $y$  with the stress free condition at infinity, we obtain the condition

$$\Sigma_{xy}^0 = -\tan \theta \Sigma_{yy}^0. \quad (3.7)$$

From (3.4)-(3.7) and the constitutive relations, we have

$$\nu'_0(y) = -\frac{f_1^0 T'_0 + \nu_0 \cos \theta}{f_{1,\nu}^0 T_0}, \quad (3.8)$$

$$u'_0(y) = \frac{f_1^0 T_0^{1/2}}{f_2^0} \tan \theta, \quad (3.9)$$

$$T''_0(y) = \frac{1}{f_4^0} \left[ (1 - e_p^2) f_5^0 T_0 - f_2^0 u'_0 - f_{4,\nu}^0 \nu'_0 T'_0 - \frac{(T'_0)^2}{2T_0} f_4^0 \right], \quad (3.10)$$

where  $f_i^0 \equiv f_i(\nu_0)$ ,  $f_{i,\nu}^0 \equiv \frac{d}{d\nu} f_i(\nu)|_{\nu=\nu_0}$ , and the prime indicates the derivative by its argument.

The boundary conditions (2.9) and (2.10) at the floor ( $y = 0$ ) for the steady uniform solution can be written as

$$T_0 = \left( \frac{\phi f_2^0 f_7^0}{f_1^0 \tan \theta} u_0 \right)^2, \quad (3.11)$$

$$T'_0 = -f_6^0 \left( \frac{1}{3} \phi u_0^2 - \frac{1}{2} \Phi T_0 \right). \quad (3.12)$$

The boundary condition (2.15) that the stress and the energy flux should vanish at infinity is satisfied when (Ahn, Brennen & Sabersky 1992)

$$T'_0(y) \rightarrow 0 \quad \text{when} \quad y \rightarrow \infty. \quad (3.13)$$

In order to obtain the steady solutions, we integrate (3.8), (3.9), and (3.10) numerically using the fourth-order Runge-Kutta method with the boundary conditions (3.11) and

(a)

(b)

(c)

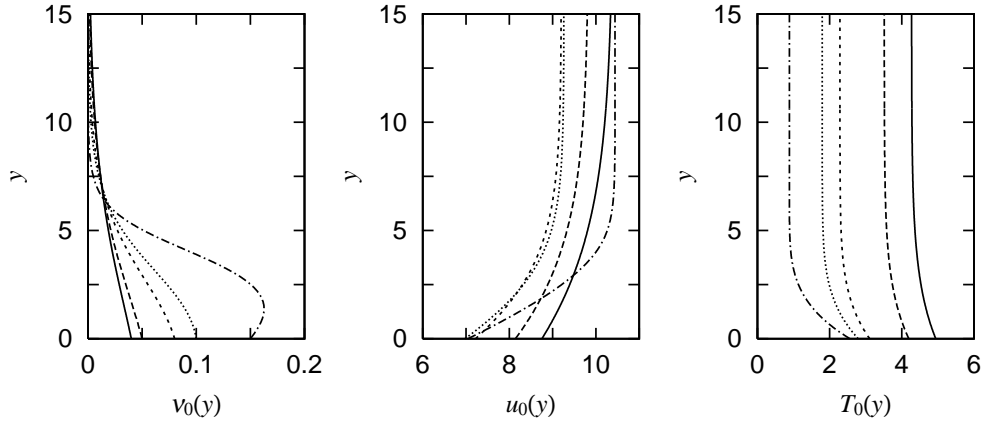


FIGURE 2. The steady solutions for  $\phi = 0.05$  and  $\theta = 16^\circ$ ; the density profiles (a), the velocity profiles (b), and the temperature profiles (c). Different line types correspond to the solutions with different densities;  $\nu_0(0) = 0.04$  (solid lines), 0.05 (long-dashed lines), 0.08 (short-dashed lines), 0.10 (dotted lines), and 0.15 (dash-dotted lines).

(3.12). We employ the shooting method to find the solution which satisfies the condition (3.13) (Forterre & Pouliquen 2002); for a given inclination angle  $\theta$  and a given density at the floor  $\nu_0(0)$ , we search for a solution by adjusting the value of the velocity at the floor  $u_0(0)$ . In the actual calculations, we integrate the equations numerically from  $y = 0$  to a certain height  $y_{\max}$ , and search for the solution which gives  $|T'_0(y_{\max})| < 10^{-8}$ . The value of  $y_{\max}$  is chosen to be large enough in comparison with the relaxation length, that depends on the parameters and can be determined only after the solution is obtained.

We use  $\theta$  and  $\nu_0(0)$  to specify the solution in the rest of the paper.

### 3.2. Numerical solutions

For a given roughness  $\phi$  of the slope, steady solutions exist for a certain range of the inclination angle of the slope  $\theta$  (Forterre & Pouliquen 2002). We present the steady solutions for the two cases, (i)  $\phi=0.05$  and (ii)  $\phi = 0.10$ ; the most of the results are for the case of  $\phi = 0.05$ , and the case of  $\phi = 0.10$  will be given to examine general trend.

(i) *The case of  $\phi = 0.05$ :* We find the steady solution for the range  $14^\circ \lesssim \theta \lesssim 19^\circ$ , but near the lower limit of  $\theta$ , the density decays with the length scale shorter than the particle diameter in the  $y$  direction, while the decay length of density becomes very large near the upper limit of  $\theta$ . In the following, we examine the solutions for  $15^\circ \lesssim \theta \lesssim 17^\circ$ .

The profiles of the density, the velocity, and the temperature for  $\theta = 16^\circ$  are shown in figure 2 for the density at the floor  $\nu_0(0) = 0.04 \sim 0.15$ . We see in the density profiles (figure 2 (a)) that the density decays monotonically when the density at the floor  $\nu_0(0)$  is small enough ( $\nu_0(0) \leq 0.10$ ), while for higher density ( $\nu_0(0) = 0.15$ ) the maximum density appears at a finite height. We focus on the lower density region because the density decays monotonically in our previous simulation (Mitarai & Nakanishi 2001; Mitarai *et al.* 2002). We notice the general tendency that the higher density flow shows lower flowing speed and the lower temperature except for the highest density case of  $\nu_0(0) = 0.15$ , where the density profile is not monotonic and the flowing speed gets faster. The general tendency is found to hold for the whole examined region ( $15^\circ \lesssim \theta \lesssim 17^\circ$ ).

(ii) *The case of  $\phi = 0.10$ :* The slope is rougher than the previous case, and the steady solution exists for  $16^\circ \lesssim \theta \lesssim 24^\circ$ . We examined the two values of the slope, i.e.,  $\theta = 20^\circ$

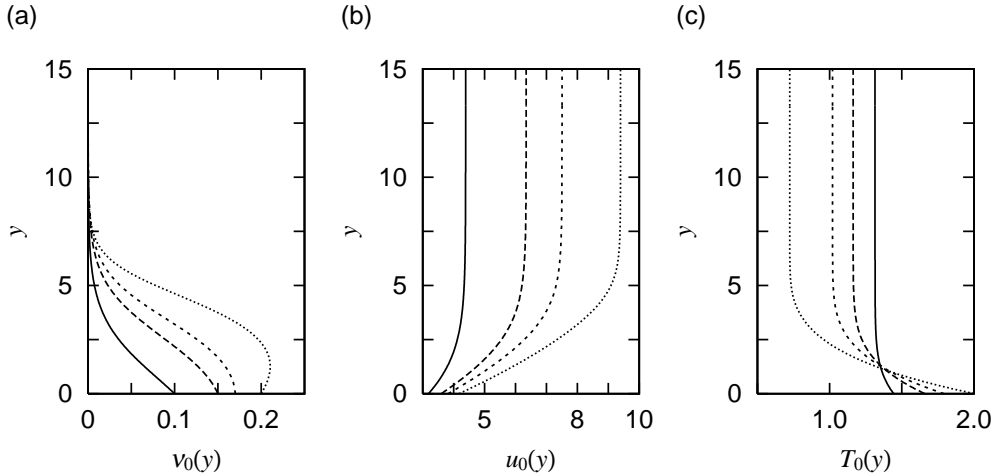


FIGURE 3. The steady solutions for  $\phi = 0.10$  and  $\theta = 20^\circ$ . The density profiles (a), the velocity profiles (b), and the temperature profiles (c). Different line types correspond to the solutions with different densities;  $\nu_0(0) = 0.10$  (solid lines), 0.15 (long-dashed lines), 0.17 (short-dashed lines), and 0.20 (dotted lines).

and  $\theta = 22^\circ$ . In the case of  $\theta = 22^\circ$ , the flowing behavior is similar with the case (i) in the lower density region, namely, the denser flow flows slower with lower temperature. In the case of  $\theta = 20^\circ$ , however, the situation is different (figure 3). The denser flow moves faster even in the lower density region where the density profile is monotonic. The denser flow has higher temperature near the bottom, while it has lower temperature for  $y \gtrsim 2$ .

#### 4. Linear Stability Analysis; Density Wave Formation

##### 4.1. Normal mode analysis

We restrict our stability analysis to the perturbation uniform along the  $z$  direction, because we are interested in the instability along the flow direction. The flow is perturbed around the steady solution as

$$\nu(x, y, t) = \nu_0(y) + \nu_1(x, y, t), \quad (4.1)$$

$$\mathbf{u}(x, y, t) = (u_0(y), 0, 0) + (u_1(x, y, t), v_1(x, y, t), 0), \quad (4.2)$$

$$T(x, y, t) = T_0(y) + T_1(x, y, t). \quad (4.3)$$

The governing equations and the boundary conditions are linearized with respect to the deviations  $\nu_1$ ,  $u_1$ ,  $v_1$ , and  $T_1$ , but the resulting expressions are rather lengthy and given in Appendix.

Now we look for the normal modes for the density, the velocity, and the temperature perturbations of the form

$$(\nu_1, u_1, v_1, T_1) = \text{Re} \left[ \left( \hat{\nu}(y), \hat{u}(y), \hat{v}(y), \hat{T}(y) \right) \exp(\alpha t + ikx) \right]. \quad (4.4)$$

The flow is linearly unstable if  $\text{Re}(\alpha) > 0$ .

As for the boundary condition at the free surface, the asymptotic behavior of the perturbations at large  $y$  are used. When  $y$  is much larger than the decay length of the density and thus  $\nu_0(y)$  is very small, the density perturbation should also decay ( $\hat{\nu} \propto \nu_0$ ), and  $\hat{u}$ ,  $\hat{v}$ , and  $\hat{T}$  decay proportional to  $\exp(-ky)$  (Forterre & Pouliquen 2002), therefore,

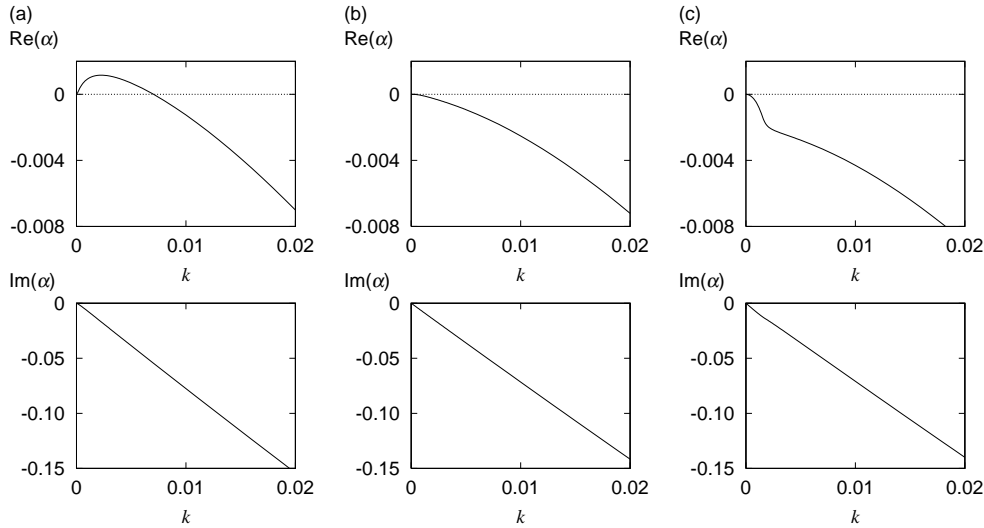


FIGURE 4. The dispersion relations of the least stable mode for the steady solutions with  $\phi = 0.05$  and  $\theta = 16^\circ$  for  $\nu_0(0) = 0.05$  (a), 0.08 (b), and 0.10 (c).

we imposed the boundary condition that

$$\hat{u}'(y) = -k\hat{u}(y), \quad \hat{v}'(y) = -k\hat{v}(y), \quad \hat{T}'(y) = -k\hat{T}(y), \quad (4.5)$$

at  $y = y_{\max}$ ;  $y_{\max}$  is a large enough height where  $\nu_0(y_{\max}) < 10^{-9}$ , in addition to the condition  $|T'_0(y_{\max})| < 10^{-8}$  discussed in §3.

We solve the eigenvalue problems of the linearized equations (A 1)-(A 4) for (4.4) numerically using the Chebychev collocation method with the discretization in the  $y$  direction (Gottlieb, Hussaini & Orsag 1984; Canuto *et al.* 1988; Boyd 2001; Foterre & Pouliquen 2002). It is known that the straightforward discretization of space requires two extra boundary conditions (Malik 1990; Foterre & Pouliquen 2002), for which we use the momentum balance condition in the  $y$  direction at  $y = 0$  and the decay condition for the density perturbation, i.e.,  $\hat{\nu}'(y) = -(\cos\theta/T_0(y))\hat{\nu}(y)$  at  $y = y_{\max}$ . In actual numerics to solve the generalized eigenvalue problem in the form  $AV = \alpha BV$  for the complex eigenvalues  $\alpha$  and the eigenvectors  $V$ , we used LAPACK version 3.0 (Anderson *et al.* 1999). The number of discretization  $N_d$  is about 100.

The numerically obtained eigenmodes contains unphysical modes, called spurious modes, due to the discretization (Mayer & Powell 1992; Boyd 2001; Foterre & Pouliquen 2002). For the spurious modes, it is known that the Chebychev coefficients of higher wave number are large, and the eigenvalues are sensitive to small change of  $N_d$ . We determine the eigenmodes as physical ones by checking that their Chebychev coefficients for higher wave number are small and their eigenvalues varies little upon changing  $N_d$ : We confirmed that, for these modes, the highest ten coefficients are less than  $10^{-7}$  when the eigenvectors are normalized so that the sum of the absolute values of the real part and the imaginary part of the largest component becomes one, and the variation of the eigenvalues by the small change of  $N_d$  are less than  $10^{-7}$ .

#### 4.2. Dispersion relations and eigenfunctions

We present the results of the linear stability analysis for the case of (i)  $\phi = 0.05$  and (ii)  $\phi = 0.10$ , for which the steady solutions are shown in §3.2; As in §3.2, most of the results are for  $\phi = 0.05$ .

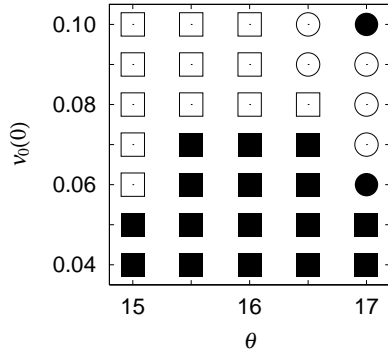


FIGURE 5. The stability diagram for  $\theta$  vs.  $\nu_0(0)$  for  $\phi = 0.05$ . The box indicates that the density profile at that point is the monotonically decaying one, while the circle represents the non-monotonic density profile. The filled (open) marks denote the region where the solution are linearly unstable (stable).

(i) *The case of  $\phi = 0.05$ :* The dispersion relations for  $\theta = 16^\circ$  are shown in figure 4 for  $\nu_0(0) = 0.05$  (a), 0.08 (b), and 0.10 (c). The growth rate  $\text{Re}(\alpha)$  is positive for  $\nu_0(0) = 0.05$  for  $0 < k \leq k_c$  with  $k_c \sim 0.007$  (figure 4(a)). As  $\nu_0(0)$  is increased, the maximum value of  $\text{Re}(\alpha)$  decreases and becomes negative for all  $k$  (figure 4(b) and (c)). We found that the solution with  $\nu_0(0) \leq 0.79$  has positive  $\text{Re}(\alpha)$  for small  $k$ , namely, the solution with low enough density is unstable against the long-wavelength perturbations. The linear dependence of  $\text{Im}(\alpha)$  on  $k$  with the negative gradient means that the least stable mode travels downstream.

The stability diagram is given in figure 5 in the parameter space of  $\theta$  vs  $\nu_0(0)$ . The boxes represent that the density profile is monotonic in the steady flow, and the circles corresponds to the non-monotonic density profile. The unstable (stable) region is shown by filled (open) marks. We find the tendency that the solution with lower density is less stable, except for the case of  $\theta = 17^\circ$ , where the non-monotonic density profile solution is found to be unstable at the highest calculated density.

The least stable eigenmodes for  $\theta = 16^\circ$  at  $k = 0.002$  are shown for the two cases: the stable case of  $\nu_0(0) = 0.10$  (figure 6) and the unstable case of  $\nu_0(0) = 0.05$  (figure 7), over one wavelength  $\lambda = 2\pi/k$ . The contours in figures 6 (a) and 7 (a) show the density eigenfunctions; the brighter (darker) regions indicate the positive (negative) regions, and the arrows represent the corresponding velocity eigenfunctions. In the both figures near  $y = 0$ , we see that the velocity perturbations point to the positive (negative)  $x$  direction in the regions of negative (positive) density perturbation. The contours for the corresponding temperature eigenfunctions plotted in figures 6(b) and 7(b) show that the regions where the density perturbation is negative (darker regions in figures 6(a) and 7(a)) roughly correspond to the positive temperature perturbations (brighter regions in figures 6(b) and 7(b)).

The difference between the stable mode (figure 6) and the unstable mode (figure 7) is seen if we focus on the divergence of velocity perturbation. In the case of the stable mode for  $\nu_0(0) = 0.10$  (figure 6(a)), the grains flow into the region where the density perturbation is negative (see the region around  $x \sim \lambda/2$  and  $y \sim 2$ ), thus the density perturbation has negative feedback. On the other hand, in the case of unstable mode for  $\nu_0(0) = 0.05$  (figure 7(a)), the grains flow into the region where the density perturbation is positive (see the region around  $x \sim 0$  and  $y \sim 3$ ); As a result, the perturbation grows and eventually causes the nonlinear density wave.

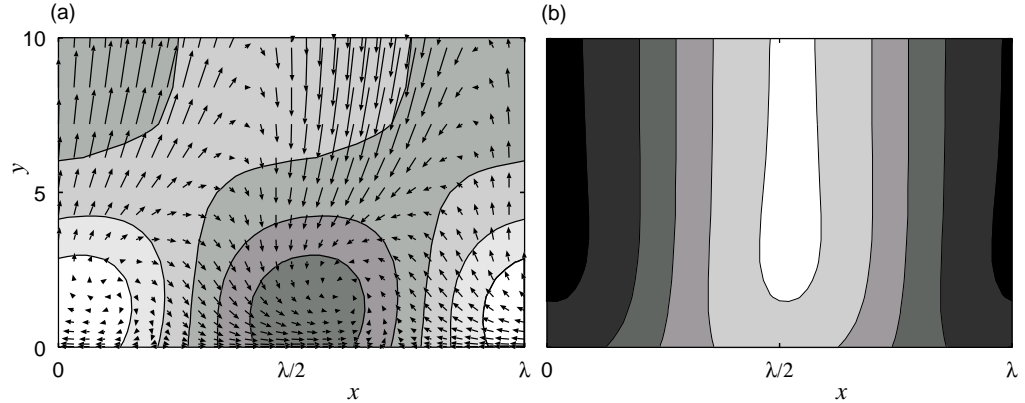


FIGURE 6. The eigenfunctions of the least stable mode for  $\phi = 0.05$ ,  $\theta = 16^\circ$ , and  $\nu_0(0) = 0.10$ , whose wave number is  $k = 0.002$ .  $\lambda$  is the wavelength of this eigenmode,  $\lambda = 2\pi/k$ . The contour of the density and the temperature eigenfunctions are shown in (a) and (b), respectively, by grey scale, where the brighter (darker) region corresponds to the larger positive (negative) value. The arrows in (a) indicate the corresponding velocity eigenfunction. It shows that the grains flow from the brighter region into the darker density region, namely, the density perturbation decays. Note that the temperature perturbation is negative at the region of the positive density perturbation.

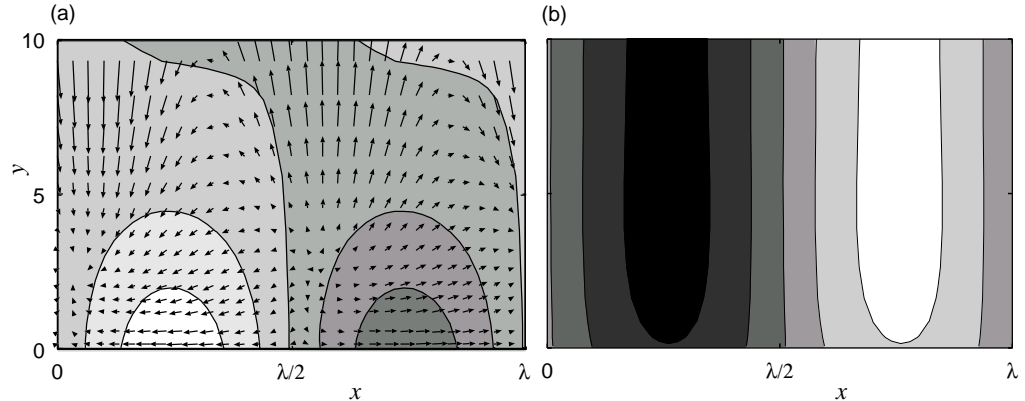


FIGURE 7. The eigenfunctions of the unstable mode for  $\phi = 0.05$ ,  $\theta = 16^\circ$ , and  $\nu_0(0) = 0.05$ , whose wave number is  $k = 0.002$ . The contour of the density eigenfunction and the velocity eigenfunction in (a) show that the grains flow from the region of negative density perturbation into that of positive perturbation, namely, the perturbation is amplified and results in the formation of the density wave. The temperature perturbation in (b) is negative at the region of positive density perturbation.

(ii) *The case of  $\phi = 0.10$ :* For  $\theta = 22^\circ$ , where the steady flow shows similar behavior to the case of (i), the tendency of the linear stability is also similar; the lower density flow is less stable. On the other hand, for  $\theta = 20^\circ$ , where the steady solutions are different, we find that the linear stability also shows a different tendency. The dispersion relations in figure 8 show that the solutions for  $\nu_0(0) = 0.10$  and  $\nu_0(0) = 0.15$  are stable (figures 8(a) and (b)), while the one for  $\nu_0(0) = 0.17$  is unstable against the long-wavelength perturbation (figure 8(c)). Namely, the solution with higher density is less stable.

The unstable eigenmodes for  $\nu_0(0) = 0.17$  with  $k = 0.002$  are shown in figure 9. The density and the velocity eigenfunctions indicate that the grains flow into the the region of positive density perturbation (see the region around  $x \sim \lambda/2$ ,  $y \sim 0$ ; the magnification

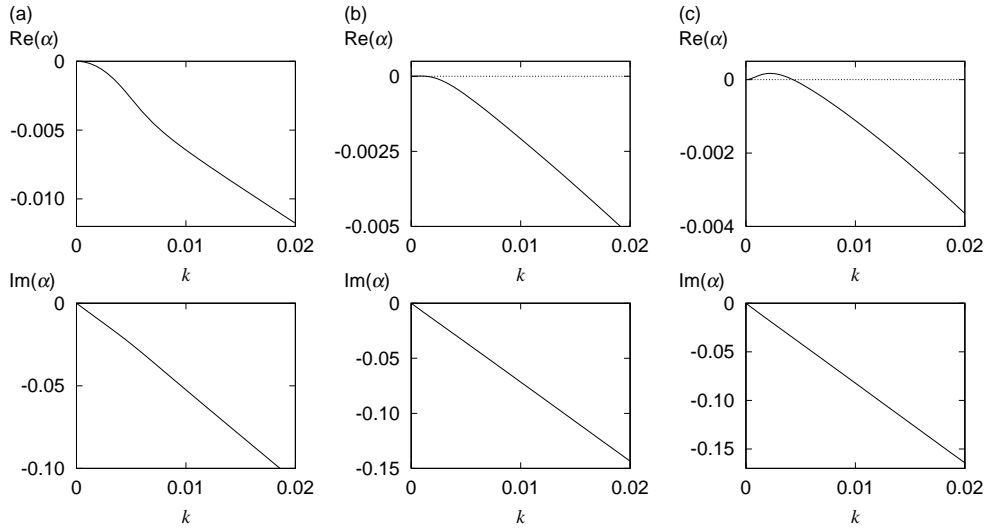


FIGURE 8. The dispersion relations of the least stable mode with  $\phi = 0.10$  and  $\theta = 20^\circ$ , for  $\nu_0(0) = 0.10$  (a), 0.15 (b), and 0.17 (c).

is shown (c)), thus the density perturbation will grow. The difference from the case (i) is that the velocity perturbation at the floor ( $y = 0$ ) is in the positive  $x$  direction in the region of the positive density perturbation; namely, the particles flow faster in the region where they get dense.

## 5. Discussions

We have calculated the steady flow solutions and examined their linear stability under the longitudinal perturbation in the cases of (i)  $\phi = 0.05$  and (ii)  $\phi = 0.10$ . In this section, we first discuss the general trend found in the steady flow, and then give a physical interpretation of the linear stability. Secondly, we compare the results with our previous simulation. Finally, we discuss the relation between our results and the stability analysis against the transverse perturbations by Forterre & Pouliquen(2002).

### 5.1. $\nu_0(0)$ dependence of the flowing speed

It has been found in §3 for  $\phi = 0.05$  and  $15^\circ \leq \theta \leq 17^\circ$  that the higher density flow shows the slower flowing speed and the lower temperature, except for the highest density case, where the flow speed gets faster and the density profile is not monotonic.

The flowing speed is determined by the balance between the gravitational force and the drag force due to the collision with the floor. The gravitational force is proportional to the total mass, while the drag force increases as the density at the floor  $\nu_0(0)$  becomes larger (see (2.9) and (2.13)). In the parameter region examined, the total mass is the increasing function of the density at the floor  $\nu_0(0)$ , therefore, both of the forces are the increasing functions of  $\nu_0(0)$ .

The trend that the higher density flow flows slower in the case of  $\phi = 0.05$  means that the increase of the drag force is larger than that of the mass upon increasing  $\nu_0(0)$ . The slower flow speed results in smaller agitation at the floor thus the lower temperature.

The opposite trend seen in the case of  $\phi = 0.10$  at  $\theta = 20^\circ$  means that the mass outgrows the drag force upon increasing  $\nu_0(0)$ ; This is more likely to happen in the case

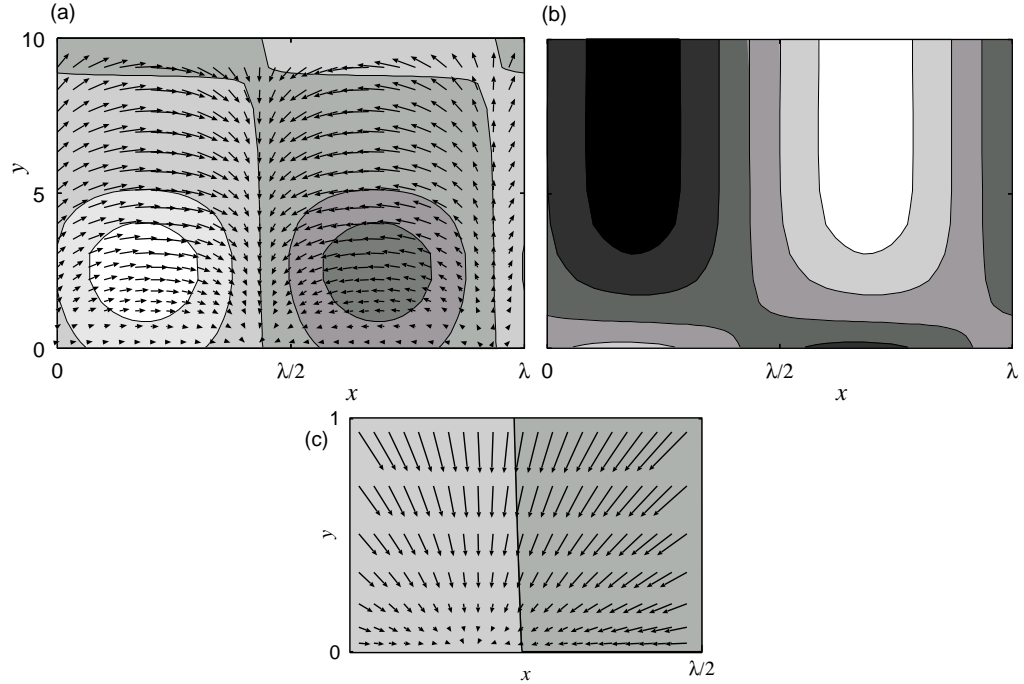


FIGURE 9. The eigenfunctions of the unstable mode for  $\phi = 0.10$ ,  $\theta = 20^\circ$ , and  $\nu_0(0) = 0.17$ , whose wave number is  $k = 0.002$ . The contour of the density eigenfunction and the velocity eigenfunction in (a) show that the grains flow into the the region of the positive density perturbation. In (b), the contour of the temperature perturbation is shown. (c) is the magnification of (a) around  $x \sim \lambda/2$ ,  $y \sim 1$ .

where the mass is large and/or the temperature is low because the drag force is not effective in these cases.

### 5.2. Mechanism of the instability

The linear stability analysis shows that the lower density flow is less stable for  $\phi = 0.05$  against the longitudinal long-wavelength perturbation, and the obtained unstable eigenmodes imply that the instability will cause the density wave. On the other hand, in the case of  $\phi = 0.10$  and  $\theta = 20^\circ$ , the higher density solution turned out to be less stable.

In order to understand this instability, it would be helpful to consider the analogy to the granular flow in a narrow vertical pipe, which is also known to form the density wave; the phenomenon has been examined experimentally (Horikawa *et al.* 1996; Raafat, Hulin & Herrmann 1996; Moriyama *et al.* 1998), numerically (Pöschel 1994; Peng & Herrmann 1995), and theoretically (Moriyama *et al.* 1998; Valance & Le Pennec 1998). The stability of the uniform flow has been found to depend on the particle density or the flow rate, although some other factors such as the particle inelasticity, the wall roughness, or the drag force by the fluid (e.g. the air), also seem to have some effects. Moriyama *et al.* (1998) have analyzed this instability by a one dimensional phenomenological model in which they take into account the drag force by the air and the relaxation process to a terminal velocity determined by the local density. It has been shown that the linear instability of the uniform flow against the long-wavelength perturbation results in the density wave formation.

This model of the pipe flow is mathematically similar to the traffic flow models (Bando *et al.* 1995; Mitarai & Nakanishi 2000a, 2000b; Kerner & Konhäuser 1993, 1994), where the density wave is known as the traffic jam. The common features among these jam-forming models are that they are quasi-one dimensional and that an optimal velocity towards which the flow velocity relaxes has a nonlinear dependence on the local particle (or car) density. As for the flow on a slope, the flow velocity depends nonlinearly on the density as a result of the competition between the drag force and the gravitational force, as has been discussed in §5.1.

The difference from the pipe flow is the spatial dimensionality; in the slope flow, the motion in the positive  $y$  direction is allowed. If the dominant motion in the slope flow is in the  $x$  direction and thus the system can be regarded as quasi-one dimensional, then the instability may be understood as the same one as that of the pipe flow. Even this situation, the length scales in the two cases are very different: in the pipe flow, the density fluctuation causes the clogging, where the density varies with the length scale of the pipe diameter. The traffic jam also develops very sharp boundaries between the jammed and the free flow regions. On the other hand, the length scale in the slope flow is very large compared with the particle diameter. We are unable to make a clear comparison of the mathematical structure of the present hydrodynamic model directly with other jam-forming models because of its complexity.

### 5.3. Comparison with the molecular dynamics simulations

We find some qualitative agreements between the result for  $\phi = 0.05$  and our previous simulations (Mitarai & Nakanishi 2001) as follows.

Our simulations were performed for a fixed inclination angle and a particular roughness of the slope, and the periodic boundary condition was imposed along the flow direction. Within the examined parameter region, the uniform flow shows the monotonic density profile, and the flow with lower density has higher velocity.

It has been demonstrated that the density wave appears only in the very long system with low enough particle density. We have performed the simulations for several sets of slope length  $L$  and particle number  $N$ . In the case of the particle density  $N\sigma/L \sim 1.0$ , the clear density wave is not formed for  $L = 250.5\sigma$  and  $L = 501\sigma$ , whereas the density wave appears for  $L = 1002\sigma$ . Upon changing the density with a fixed system length  $L = 501\sigma$ , the density wave is formed when  $N\sigma/L \sim 0.75$ , while the uniform flow is stable when  $N\sigma/L \sim 1.0$  and 2.0.

These simulation results agree with the present model in the case of  $\phi = 0.05$  with the monotonic density profiles on the three points: (i) The flow with lower density is faster, (ii) The critical wavelength for instability is very long, and (iii) The lower density flow is less stable. Regarding (ii), the critical wave length  $\lambda_c = 2\pi/k_c$  is very long;  $\lambda_c \sim 900\sigma$  for  $\theta = 16^\circ$  and  $\nu_0(0) = 0.05$ , for example. We do not understand how such a small wave number arises, but this seems to be comparable with our simulation results, where the critical slope length  $L_c$  was between  $500\sigma$  and  $1000\sigma$  for  $N\sigma/L \sim 1.0$ .

### 5.4. Comparison with the stability analysis against the transverse perturbations

Forterre & Pouliquen (2002) examined the linear stability of the granular flow on a wide slope against the perturbation transverse to the flowing direction, in order to understand the regular streak pattern along the flow direction observed in their experiments (Forterre & Pouliquen 2001). They mainly focused on the parameter region where the non-monotonic density profile (or what they call the “inverted density profile”) is observed, because, from the analogy to the Rayleigh-Bénard instability, they expected that such a flow would be unstable to form the convection rolls. They have shown that, in the large part of

the parameter region where the inverted density profile is observed, the flow is unstable against the transverse perturbation. The unstable mode shows the vortex-like pattern, and they concluded that the streaks observed in the experiments result from the rolls of vortices. They also found that the flow with the monotonic density profile becomes unstable for some parameters, but the detail has not been reported.

If the transverse instability is the Rayleigh-Bernard type as suggested by Forterre & Pouliquen (2002), it should be different from the longitudinal jamming instability analyzed here. It should be interesting to study how the two instabilities interfere with each other or not by the full three dimensional analysis. In this regard, the square lattice pattern found in the large inclination angle is very interesting (Forterre & Pouliquen 2002).

## 6. Summary

The steady flows and their linear stability are analyzed for the granular flow on a slope using the hydrodynamic model with the constitutive relations derived from the kinetic theory of inelastic spheres. We focused on the relatively low density region where the density decays monotonically.

For the case with the roughness  $\phi = 0.05$ , it was shown that the lower density flow is faster and less stable against the perturbations longitudinal to the flowing direction, and that the critical wavelength of the instability is very long. By analyzing the unstable mode, it was shown that this instability results in the density wave formation. These results agree qualitatively with our previous simulations of the density wave formation on a slope.

As for the case of the roughness  $\phi = 0.10$  with  $\theta = 20^\circ$ , the flowing behavior is different; It has been found that the flow with higher density is faster and less stable. The nature of instability seems to be different for these two cases.

In our present analysis of the hydrodynamic model for the rapid flow, we obtained the parameter region of the density wave formation that agrees with our simulations, but the mathematical structure of the instability is not yet clear because the equations are rather complicated. In this respect, it is desirable to establish a formalism to simplify the model in a systematic way.

This work was partially supported by Hosokawa powder technology foundation and Grant-in-Aid for JSPS fellows.

## Appendix. Linearized equations

In this appendix, the linearized governing equations for the longitudinal perturbations (4.1)-(4.3) and the boundary conditions are given (Forterre & Pouliquen 2002, see also Alam & Nott 1998). The superscript 0 denotes that the quantities are for steady solution. The subscript  $\nu$  and  $T$  denotes the partial derivatives by the variables;  $p_\nu^0 = \partial p(\nu, T) / \partial \nu|_{\nu=\nu_0, T=T_0}$ . The subscript  $y$  indicates the total differential with respect to  $y$ , namely,  $p_y^0 = dp^0(\nu(y), T(y)) / dy = [\partial p(\nu, T) / \partial \nu|_{\nu=\nu_0, T=T_0}] \nu_{0,y} + [\partial p(\nu, T) / \partial T|_{\nu=\nu_0, T=T_0}] T_{0,y}$ ,  $\nu_{0,y} = d\nu_0(y) / dy$ , and so on.  $\partial_t$ ,  $\partial_y$ , and  $\partial_x$  represent  $\partial / \partial t$ ,  $\partial / \partial y$ , and  $\partial / \partial x$ , respectively. The expressions of  $p(\nu, T)$ ,  $\mu(\nu, T)$ ,  $\zeta(\nu, T)$ ,  $\kappa(\nu, T)$ , and  $\Gamma(\nu, T)$  are given in (2.7), and  $\xi(\nu, T) = \zeta - 2\mu/3$ . Then, by inserting (4.1)-(4.3) into (2.1)-(2.3) through (3.1)-(3.3), we obtain the following expressions;

$$\begin{aligned} [\partial_t + u_0 \partial_x] \nu_1 + [\nu_0 \partial_x] u_1 + [\nu_{0,y} + \nu_0 \partial_y] v_1 &= 0, \\ [\sin \theta - p_\nu^0 \partial_x + u_{0,yy} \mu_\nu^0 + u_{0,y} \mu_{\nu,y}^0 + u_{0,y} \mu_\nu^0 \partial_y] \nu_1 \end{aligned} \quad (\text{A } 1)$$

$$\begin{aligned}
& + [-\nu_0 \partial_t - \nu_0 u_0 \partial_x + (\xi^0 + 2\mu^0) \partial_x^2 + \mu_y^0 \partial_y + \mu^0 \partial_y^2] u_1 \\
& + [-\nu_0 u_{0,y} + \mu_y^0 \partial_x + (\xi^0 + \mu_0) \partial_x \partial_y] v_1 \\
& + [-p_T^0 \partial_x + u_{0,yy} \mu_T^0 + u_{0,y} \mu_{T,y}^0 + u_{0,y} \mu_T^0 \partial_y] T_1 = 0,
\end{aligned} \tag{A 2}$$

$$\begin{aligned}
& [-\cos \theta - p_{\nu y}^0 - p_{\nu}^0 \partial_y + u_{0,y} \mu_{\nu}^0 \partial_x] \nu_1 \\
& + [\xi_y^0 \partial_x + \xi^0 \partial_x \partial_y + \mu^0 \partial_x \partial_y] u_1 \\
& + [-\nu_0 \partial_t - \nu_0 u_0 \partial_x + \xi_y^0 \partial_y + \xi^0 \partial_y^2 + 2\mu_y^0 \partial_y + 2\mu_0 \partial_y^2 + \mu_0 \partial_x^2] v_1 \\
& + [-p_{T,y}^0 - p_T^0 \partial_y + u_{0,y} \mu_T^0 \partial_x] T_1 = 0,
\end{aligned} \tag{A 3}$$

$$\begin{aligned}
& [\kappa_{\nu y}^0 T_{0,y} + \kappa_{\nu}^0 T_{0,yy} + \kappa_{\nu}^0 T_{0,y} \partial_y - \Gamma_{\nu}^0 + u_{0,y}^2 \mu_{\nu}^0] \nu_1 \\
& + [-p^0 \partial_x + 2\mu^0 u_{0,y} \partial_y] u_1 \\
& + \left[ -\frac{3}{2} \nu_0 T_{0,y} - p^0 \partial_y + 2\mu^0 u_{0,y} \partial_x \right] v_1 \\
& + \left[ -\frac{3}{2} \nu_0 \partial_t - \frac{3}{2} \nu_0 u_0 \partial_x + \kappa^0 \partial_x^2 + \kappa_y^0 \partial_y + \kappa^0 \partial_y^2 \right. \\
& \left. + \kappa_{T,y}^0 T_{0,y} + \kappa_T^0 T_{0,yy} + \kappa_T^0 T_{0,y} \partial_y - \Gamma_T^0 + u_{0,y}^2 \mu_T^0 \right] T_1 = 0.
\end{aligned} \tag{A 4}$$

The linearized boundary conditions at  $y = 0$  are obtained from (2.9) and (2.10) as

$$\partial_y u_1 = \phi [u_0 f_{7,\nu}^0 \nu_1 + f_7^0 u_1], \tag{A 5}$$

$$\partial_y T_1 = -f_{6,\nu}^0 \left[ \frac{1}{3} \phi u_0^2 - \frac{1}{2} \Phi T_0 \right] \nu_1 - f_6^0 \left[ \frac{2}{3} \phi u_0 u_1 - \frac{1}{2} \Phi T_1 \right]. \tag{A 6}$$

## REFERENCES

AHN, H., BRENNEN, C. E. & SABERSKY, R. H. 1992 Analysis of the fully developed chute flow of granular materials. *J. Appl. Mech.* **59**, 109–119.

ALAM, M. & NOTT, P. R. 1998 Stability of plane Couette flow of a granular material. *J. Fluid Mech.* **377**, 99–136.

ANDERSON, E., BAI, Z., BISCHOF, C., BLACKFORD, S., DEMMEL, J., DONGARRA, J., DU CROZ, J., GREENBAUM, A., HAMMARLING, S., MCKENNEY, A. & SORENSEN, D. 1999 *LAPACK Users' Guide*, 3rd edn. Philadelphia, PA: Society for Industrial and Applied Mathematics.

BANDO, M., HASEBE, K., NAKAYAMA, A., SHIBATA, A., & SUGIYAMA, A. 1995 Dynamical model of traffic congestion and numerical simulation. *Phys. Rev. E* **51**, 1035–1042.

BOYD, J. P. 2001 *Chebyshev and Fourier Spectral Methods (Second Edition)*. Dover.

CAMPBELL, C. S. 1990 Rapid granular flows. *Ann. Rev. Fluid Mech.* **22**, 57–92.

CANUTO, C., HUSSAINI, M. Y., QUARTERONI, A. & ZANG, T. A. 1988 *Spectral Methods in Fluid Dynamics*. Springer Series in computational physics.

CUNDALL, P. A. & STRACK, O. D. L. 1979 A discrete numerical model for granular assemblies. *Geotechnique* **29**, 47–65.

FORTERRE, Y. & POULIQUEN, O. 2001 Longitudinal vortices in granular flows. *Phys. Rev. Lett.* **86**, 5886–5889.

FORTERRE, Y. & POULIQUEN, O. 2002 Stability analysis of rapid granular chute flows: formation of longitudinal vortices. *J. Fluid Mech.* **467**, 361–387.

GOTTILIEB, D., HUSSAINI, M. Y. & ORSAG, S. A. 1984 Theory and applications of spectral methods. In *Spectral Methods for Partial Differential Equations* (ed. R. G. Voigt, D. Gottlieb & M. Y. Hussaini). SIAM.

HORIKAWA, S., ISODA, T., NAKAYAMA, T., NAKAHARA, A., & MATSUSHITA, M. 1996 Self-organized critical density waves of granular particles flowing through a pipe. *Physica A* **233**, 699–708.

JAEGER, H. M., NAGEL, S. R. & BEHRINGER, R. P. 1996 Granular solids, liquids, and gases. *Rev. Mod. Phys.* **68** (4), 1259.

JENKINS, J. T. 1992 Boundary conditions for rapid granular flow: flat, frictional walls. *J. Appl. Mech.* **59**, 120–127.

JENKINS, J. T. & RICHMAN, M. W. 1986 Boundary conditions for plane flows of smooth, nearly elastic, circular disks. *J. Fluid Mech.* **171**, 53–69.

JENKINS, J. T. & SAVAGE, S. B. 1983 A theory for the rapid flow of identical, smooth, nearly elastic, spherical particles. *J. Fluid Mech.* **130**, 187–202.

JOHNSON, P. C. & JACKSON, R. 1987 Frictional-collisional constitutive relations for granular materials, with application to plane shearing. *J. Fluid Mech.* **176**, 67–93.

JOHNSON, P. C., NOTT, P. & JACKSON, R. 1990 Frictional-collisional equations of motion for particulate flows and their application to chutes. *J. Fluid Mech.* **210**, 501–535.

KERNER, B. S. & KONHÄUSER, P. 1993 Cluster effect in initially homogeneous traffic flow. *Phys. Rev. E* **48**, R2335–R2338.

KERNER, B. S. & KONHÄUSER, P. 1994 Structure and parameters of clusters in traffic flow. *Phys. Rev. E* **50**, 54–83.

LOUGE, M. Y. & KEAST, S. C. 2001 On dense granular flows down flat frictional inclines. *Phys. Fluids* **13**, 1213–1233.

LUN, C. K. K. & SAVAGE, S. B. 1986 The effects of an impact velocity dependent coefficient of restitution on stresses developed by sheared granular materials. *Acta Mech.* **63**, 15–44.

LUN, C. K. K., SAVAGE, S. B., JEFFREY, D. J. & CEPURNIY, N. 1984 Kinetic theories for granular flow: inelastic particles in Couette flow and slightly inelastic particles in a general flowfield. *J. Fluid Mech.* **223**, 223–256.

MALIK, M. R. 1990 Numerical methods for hypersonic boundary layer stability. *J. Comput. Phys.* **86**, 376–413.

MAYER, E. W. & POWELL, K. G. 1992 Viscous and inviscid instabilities of a trailing vortex. *J. Fluid Mech.* **245**, 91–114.

MITARAI, N., HAYAKAWA, H. & NAKANISHI, H. 2002 Collisional granular flow as a micropolar fluid. *Phys. Rev. Lett.* **88**, 174301.

MITARAI, N. & NAKANISHI, H. 2000a Convective instability and structure formation in traffic flow. *J. Phys. Soc. Jpn* **69**, 3752–3761.

MITARAI, N. & NAKANISHI, H. 2000b Spatiotemporal structure of traffic flow in a system with an open boundary. *Phys. Rev. Lett.* **85**, 1766–1769.

MITARAI, N. & NAKANISHI, H. 2001 Instability of dilute granular flows on rough slope. *J. Phys. Soc. Jpn.* **70**, 2809–2812.

MITARAI, N. & NAKANISHI, H. 2003 Hard-sphere limit of soft-sphere model for granular materials: Stiffness dependence of steady granular flow. *Phys. Rev. E* **67**, 021301.

MORIYAMA, O., KUROIWA, N., MATSUSHITA, M. & HAYAKAWA, H. 1998 4/3 law of granular particles flowing through a vertical pipe. *Phys. Rev. Lett.* **80**, 2833–2836.

PENG, G. & HERRMANN, H. J. 1995 Density waves and 1/f density fluctuations in granular flow. *Phys. Rev. E* **51**, 1745–1756.

POULIQUEN, O. 1999 Scaling laws in granular flows down rough inclined planes. *Phys. Fluids* **11**, 542–545.

PÖSHEL, T. 1994 Recurrent clogging and density waves in granular material flowing through a narrow pipe. *J. Phys. I France* **4**, 499–506.

PRASAD, S. N., PAL, D. & RÖMKENS, M. J. M. 2000 Wave formation on a shallow layer of flowing grains. *J. Fluid Mech.* **413**, 89–110.

RAAFAT, T., HULIN, J. P. & HERRMANN, H. J. 1996 Density waves in dry granular media falling through a vertical pipe. *Phys. Rev. E* **53**, 4345–4350.

RICHMAN, M. W. 1988 Boundary conditions based upon a modified Maxwellian velocity distribution for flows of identical, smooth, nearly elastic spheres. *Acta Mechanica* **75**, 227–240.

VALANCE, A. & PENNEC, T. L. 1998 Nonlinear dynamics of density waves in granular flows through narrow vertical channels. *Euro. Phys. J. B* **5**, 223–229.